

FeS₂ monolayer: a high valence and high- T_C Ising ferromagnet

Ke Yang,^{1,2} Yaozhenghang Ma,² Lu Liu,² Yueyue Ning,¹ Di Lu,² Yuxuan Zhou,² Zhongyao Li,¹ and Hua Wu^{2,3,4,*}

¹College of Science, University of Shanghai for Science and Technology, Shanghai 200093, China

²Laboratory for Computational Physical Sciences (MOE), State Key Laboratory of Surface Physics, and Department of Physics, Fudan University, Shanghai 200433, China

³Shanghai Qi Zhi Institute, Shanghai 200232, China

⁴Collaborative Innovation Center of Advanced Microstructures, Nanjing 210093, China

(Dated: January 15, 2024)

Two-dimensional (2D) magnetic materials are of current great interest for their promising applications in spintronics. Strong magnetic coupling and anisotropy are both highly desirable for the achievement of a high temperature magnetic order. Here we propose the unusual high valent FeS₂ hexagonal monolayer as such a candidate for a strong Ising 2D ferromagnet (FM), by spin-orbital state analyses, first-principles calculations, and the renormalized spin-wave theory (RSWT). We find that very importantly, the high valent Fe⁴⁺ ion is in the low-spin state (t_{2g}^4 , $S=1$) with degenerate t_{2g} orbitals rather than the high-spin state ($t_{2g}^3 e_g^1$, $S=2$). It is the low-spin state that allows to carry a large perpendicular orbital moment and then produces a huge single ion anisotropy (SIA) of 25 meV/Fe. Moreover, the negative charge transfer character associated with the unusual high valence, strong Fe 3d-S 3p hybridization, wide bands, and a small band gap all help to establish a strong superexchange. Indeed, our first-principles calculations confirm the strong FM superexchange and the huge perpendicular SIA, both of which are further enhanced by a compressive strain. Then, our RSWT calculations predict that the FM T_C is 261 K for the pristine FeS₂ monolayer and could be increased to 409 K under the compressive -5% strain. The high T_C is also reproduced by our Monte Carlo (MC) simulations. Therefore, it is worth exploring the high- T_C Ising FMs in the high valent 2D magnetic materials with degenerate orbitals.

I. Introduction

Since the discovery of 2D FM CrI₃ [1] and Cr₂Ge₂Te₆ [2] in 2017, 2D magnetic materials have attracted great interest due to their promising applications in quantum devices and information technology [3–7]. According to the Mermin-Wagner theorem [8], magnetic anisotropy (MA) is essential for establishing a long-range magnetic order in 2D materials. Both the CrI₃ monolayer [1] and Cr₂Ge₂Te₆ bilayer [2] have a weak perpendicular MA, which was ascribed to an exchange anisotropy caused by the spin-orbit coupling (SOC) of the heavy ligand p orbitals and their hybridization with the Cr 3d orbitals [9–11]. Here the octahedral Cr³⁺ $S=3/2$ ion has a closed t_{2g}^3 shell, and its orbital singlet produces no single-ion anisotropy (SIA). In contrast, the VI₃ monolayer has an open V^{3+} t_{2g}^2 shell, which allows for an unquenched orbital moment and a large SIA of 16 meV per V^{3+} ion [12]. This accounts for the recent experimental observations of the large orbital moment and Ising magnetism in VI₃ monolayer [13–15]. As a large MA maintains a preferred magnetic orientation against the thermal fluctuation and excitation, it may stabilize a long-range magnetic order at a high temperature [1, 2, 13–20]. To facilitate practical applications of the 2D magnetic materials, it is highly desirable to achieve both a strong magnetic coupling and anisotropy in them and thus their high ordering temperature.

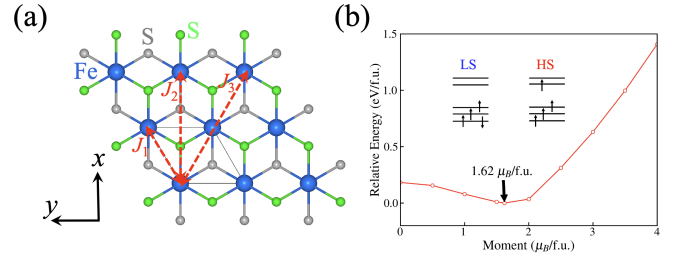


FIG. 1. (a) The crystal structure of FeS₂ monolayer. J_1 , J_2 , and J_3 refer to the first, second, and third nearest neighbor magnetic exchanges. (b) Fixed-spin-moment calculations imply the formal low-spin state with $S=1$ for Fe⁴⁺.

Very recently, an unusual high valent FeS₂ monolayer in a triangular structure was successfully synthesized using a competitive-chemical-reaction-based growth mechanism [21]. Its main structural units are the edge-sharing FeS₆ octahedra arranged into a delicate triangular network of Fe ions, as seen in Fig. 1(a). It was found to be an intriguing 2D FM semiconductor with a small band gap and a low Curie temperature ($T_C \approx 15$ K), and its analog with higher T_C may have potential applications in photodetectors and spintronic devices [21].

In contrast to a series of existing 2D magnetic materials having the normal valence states such as Cr³⁺ in CrI₃ [1] and Mn²⁺ in MnBi₂Te₄ [22, 23], FeS₂ monolayer is quite unique because of the unusual high valent Fe⁴⁺ ions. The high valence transition metal (TM) compounds often have exotic electronic states, strong covalency between the TM and ligands, and surprising magnetic properties [24–26]. Although the Hund exchange

* Corresponding author. wuh@fudan.edu.cn

favors a high-spin (HS) state with a maximal spin for $3d$ TM ions, such as Cr^{3+} $S=3/2$, Mn^{2+} $S=5/2$, Fe^{2+} $S=2$, and Fe^{3+} $S=5/2$, the octahedral Fe^{4+} ion may well be in a low-spin (LS) $S=1$ state rather than the HS $S=2$ state, as the very strong hybridization between Fe^{4+} $3d$ and S^{2-} $3p$ orbitals could dominate over the Hund exchange and then stabilize the LS state. In addition, the strong hybridization and wide band effect would narrow the band gap of semiconductors or even produce a metallic behavior, and all this would favor the magnetic couplings, either superexchange via the virtual excitation across the small band gap or the itinerant magnetism in the metallic systems. Moreover, the formal LS Fe^{4+} ($3d^4$, $S=1$) ion in the local FeS_6 octahedron has the $t_{2g}^{3\uparrow,1\downarrow}$ configuration, and the degenerate t_{2g} triplet orbitals could carry the large orbital moment $L=1$ and produce a strong SIA. Then, the pristine FeS_2 monolayer could have both the strong magnetic coupling and anisotropy, and consequently it could possess a high ordering temperature suitable for promising spintronic applications. Furthermore, we rationalize the recent experimental low T_C by demonstrating the S vacancy effect as seen below, and thus propose that the native high T_C of FeS_2 monolayer may be restored by removing the S vacancies.

The above pictures motivate us to study the electronic structure and magnetic property of FeS_2 monolayer, using the first-principles calculations, crystal-field level and spin-state diagrams, charge-transfer type superexchange analysis, and RSWT calculations. Indeed, our work confirms that the unusual high valent Fe^{4+} ion is in the LS $S=1$ state and possesses a large out SIA-of-plane orbital moment of about $1 \mu_B$ and thus a huge perpendicular of 25 meV/Fe. Moreover, we find that FeS_2 monolayer is a charge-transfer type semiconductor with a tiny band gap and has considerably strong FM couplings. Thus, the pristine FeS_2 monolayer would have quite high T_C which is even increased above room temperature under a few percent compressive strain according to our RSWT calculations and MC simulations. Therefore, this prediction calls for an experimental study, and the high valent van der Waals magnetic materials with degenerate orbitals are worth exploring in the search of the 2D high- T_C Ising ferromagnets.

II. Computational Details

We perform density functional theory (DFT) calculations using the Vienna *ab initio* simulation package (VASP) [27]. The kinetic energy cutoff for plane wave expansion is set to 500 eV. The Monkhorst-Pack grid of $11 \times 11 \times 1$ is used for 1×1 planar unit cell, and $(3 \times 3 \times 1)$ k-mesh for 4×4 planar supercell. The experimental lattice constants of $a = b = 3.23 \text{ \AA}$ [21] for FeS_2 monolayer are used in our calculations, as the DFT optimized lattice constants $a = b = 3.20 \text{ \AA}$ are almost the same as them. The atomic positions are fully relaxed till the force on each atom is less than 0.01 eV/\AA and the total energy

minimization is performed with a tolerance of 10^{-5} eV . A vacuum space larger than 15 \AA is employed to avoid periodic image interactions between FeS_2 layers. To account for the electron correlation of Fe $3d$ states, the local-spin-density approximation plus Hubbard U (LSDA + U) calculations are performed using the common value of Hubbard $U = 5 \text{ eV}$ and Hund exchange $J_H = 1 \text{ eV}$, and moreover, the hybrid functional calculations are carried out. Both the calculations give very similar band structures as seen below and also reproduce the experimental small gap. Furthermore, we test the U values in the reasonable range of 4-6 eV and find that our prediction of the quite high T_C Ising FM remains unchanged as seen below.

To check the ground state and possible metastable states of the spin-orbital system, we use the open-source software developed by Watson [28] to construct the occupation number matrices for multiple spin-orbital states, see more details in Section I of Supplemental Material (SM) [29] (see also references [21, 30–37] therein). Then, the LSDA+ U calculations read those occupation number matrices and yield the orbitally dependent/polarized potential in each iteration of electronic steps. Furthermore, those occupation number matrices are updated and read iteratively in self consistent calculations till a full electronic relaxation. Normally, in such calculations the ground state and several low-energy metastable states can be stabilized as they are, but some high-energy metastable states are too unstable to converge to the ground state or a low-energy metastable state. Then, one can determine the ground state of spin-orbital system in a reliable way using such calculations, as demonstrated in many previous works [12, 17, 20, 38, 39]. For example, such calculations can well reproduce the experimental crystal field level splitting and orbital excitation energy, and in this work their accuracy is proven by reproducing the SOC strength of the Fe^{4+} $3d$ electrons as seen below. Note also that the SOC is included for Fe and S atoms by the second-variational method with scalar relativistic wave functions. The magnetic phase transition of the FeS_2 monolayer is probed using RSWT and MC simulations, see more computational details in SM [29].

III. Results and Discussion

A. The Low-Spin State of The Fe^{4+} Ion

To clearly see the crystal field effect, exchange splitting, electron correlation, and the crucial SOC effects, we present and discuss below the LSDA and LSDA+SOC+ U calculations. We first carry out LSDA calculations to see the basic electronic structure of FeS_2 monolayer. The Fe $3d$ states in the local FeS_6 octahedron split into the higher-lying e_g^σ doublet and the lower t_{2g} triplet with the energy separation of about 2 eV, and the t_{2g} further splits into a_{1g} singlet and e_g^π doublet in the global trigonal crystal field, as seen in Fig. 2 and in section I of

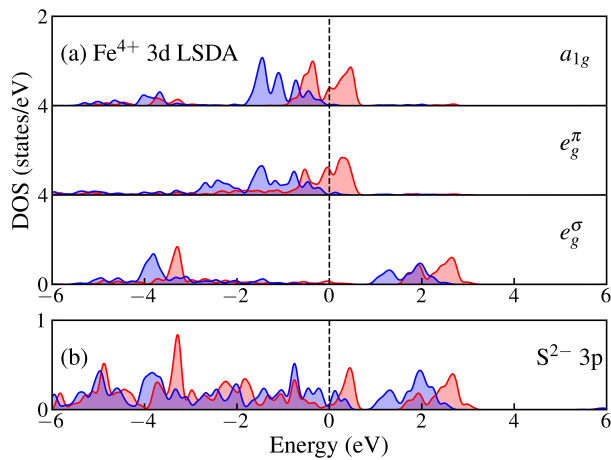


FIG. 2. (a) Fe 3d and (b) S 3p DOS by LSDA. The blue (red) curves stand for the up (down) spin channel. The Fermi level is set at zero energy.

SM [29]. The a_{1g} and e_g^π are almost degenerate and spin-polarized, with the up-spin channel being fully filled but the down-spin one partially occupied, and the e_g^σ doublet is formally unoccupied, with the antibonding state lying around 2 eV above the Fermi level. Obviously, there is a strong hybridization between the Fe 3d and S 3p states, making their broad bands distributing over a large energy range from -6 eV to 3 eV. It is the strong hybridization that produces a huge $pd\sigma$ bonding-antibonding splitting of about 6 eV (about -4 eV vs 2 eV) for the Fe 3d e_g^σ states. There are a lot of holes on the S 3p states, featuring the negative charge-transfer behavior in such unusually high valent compounds [40, 41]. The calculated local spin moment is $1.50 \mu_B$ per Fe^{4+} , implying the low-spin $S=1$ state with the formal $t_{2g}^{3\uparrow,1\downarrow}$ configuration. Owing to the strong Fe 3d-S 3p hybridization, the S 3p fat orbitals/delocalized states get also somewhat spin-polarized, having $0.03 \mu_B$ per S within its muffin-tin sphere and $0.06 \mu_B$ in the interstitial region per formula unit (fu). All those spin moments add up to the total spin moment of $1.62 \mu_B/\text{fu}$, but this moment is still reduced from the formal $\text{Fe}^{4+} S=1$ state, just by the electron itineracy in the LSDA metallic band structure originating from the strong Fe 3d-S 3p hybridization.

To double-check the possible LS ground state of the formal Fe^{4+} ion, we perform fixed-spin-moment calculations and compute the LSDA total energies for the total spin moments ranging from the nonmagnetic $S=0$ state via the LS $S=1$ to the HS $S=2$ state. As seen in Fig. 1(b), the obtained results show that the ground state indeed has a total spin moment close to $2 \mu_B/\text{fu}$ (i.e., the LS $S=1$ state), and that the HS $S=2$ state is extremely unstable, lying above the LS state too much by about 1.5 eV/fu. All the above results show that the unusual high valent Fe^{4+} ion is in the formal LS $S=1$ state rather than the HS $S=2$ state.

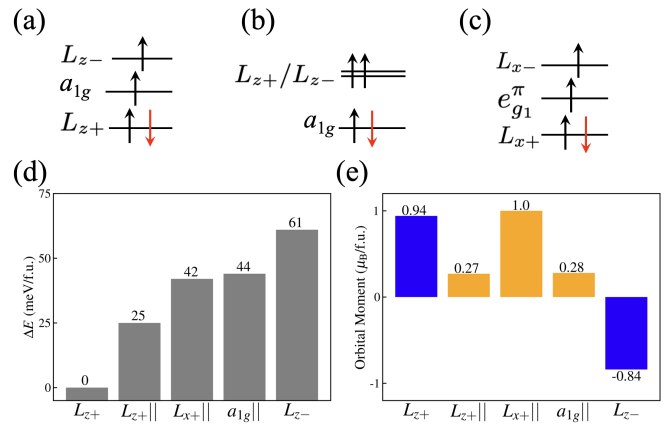


FIG. 3. Crystal field level diagrams for the LS $\text{Fe}^{4+} S = 1$ ion in different configuration states: the single down-spin electron occupies the (a) L_{z+} , (b) a_{1g} , and (c) L_{x+} states. (d) the relative total energies ΔE (meV/fu), and (e) orbital moments (blue color for out-of-plane and yellow for in-plane) for the FeS_2 monolayer in different states by LSDA+SOC+ U . The symbol \parallel in the state labellings marks the in-plane magnetization, in comparison with other states with out-of-plane magnetization.

B. The $L_z=1$ Ground State and Huge SIA

The LS Fe^{4+} ion has the formal $t_{2g}^{3\uparrow,1\downarrow}$ configuration, and the nearly degenerate a_{1g} and e_g^π orbitals in the global trigonal crystal field could make the Fe^{4+} ion stay in different orbital states, as seen in Fig. S5. Actually, all these states have the same full filling of the up-spin t_{2g} orbitals, but differ only in the occupation of the down-spin t_{2g} which is therefore used for labeling of those states. The different combinations of the a_{1g} singlet and e_g^π doublet in case of the corresponding orbital degeneracy, yield the $L_{z\pm}$, $L_{x\pm}$, or $L_{y\pm}$ state with an orbital moment of $\pm 1 \mu_B$ along the z , x , or y -axis, respectively, see Section I in SM for more details [29]. Note that the a_{1g} orbital singlet state in Fig. S5(b) formally has no orbital moment but could carry a small one due to the SOC mixing of the a_{1g} and e_g^π . Moreover, owing to the actual trigonal crystal field splitting between the a_{1g} singlet and e_g^π doublet, the real $L_{z\pm}$ and $L_{x\pm}$ states obtained below could have the orbital moment different from $\pm 1 \mu_B$ which is also spin-orientation dependent due to the SOC effect, see Fig. 3(e). By inclusion of the SOC and electron correlation effects of Fe 3d orbitals, we carry out LSDA+SOC+ U calculations to determine which one in Fig. S5(d) is the spin-orbital ground state of FeS_2 monolayer. Indeed, all these states can be stabilized in our calculations guided by the initialized occupation number matrices and by the subsequent full electronic relaxation.

All the solutions are semiconducting with a tiny band gap, and the corresponding results are displayed in Fig. 4 and Section II in SM [29]. The ground state is the L_{z+} . It has the total spin moment of $1.98 \mu_B$ and the

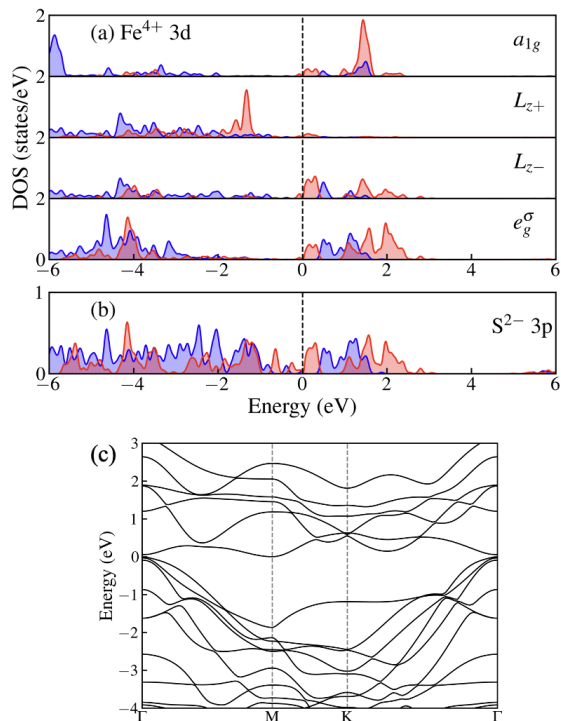


FIG. 4. (a) Fe 3d and (b) S 3p DOS of FeS₂ monolayer in the L_{z+} ground state by LSDA+SOC+ U . The blue (red) curves stand for the up (down) spin channel. The Fermi level is set at zero energy. (c) The corresponding band structure with a tiny band gap of 40 meV.

parallel orbital moment of $0.94 \mu_B$ both along the z -axis (Figs. S5a and 4). The L_{z-} state, where the orbital moment is antiparallel to the total spin moment, would lose the SOC energy and the increasing total energy of 61 meV/fu [$\Delta E = \zeta(\Delta l_z)s_z = \zeta \cdot 2 \cdot 1/2$] leads to the estimate of the SOC parameter $\zeta = 61$ meV for the formal Fe⁴⁺ ion, see Fig. S5(d). As the L_{z+} orbital moment firmly fixes via the SOC the parallel spin moment along the z -axis, and if the spin moment could be flipped into the xy plane, the total energy would rise up by 25 meV/fu (Fig. S5(d)), showing a huge SIA energy of 25 meV/Fe which approaches the ideal $\zeta/2$. Moreover, we obtain the L_{x+} state and it has both the x -axis spin moment of $2 \mu_B$ and the orbital moment of $1 \mu_B$, but its total energy is higher than the L_{z+} ground state by 42 meV/fu, see Figs. S5(d) and (e). We also get the a_{1g} state and it has a finite in-plane orbital moment of $0.28 \mu_B$ and lies above the L_{z+} ground state by 44 meV/fu.

Then, in FeS₂ monolayer, the formal Fe⁴⁺ ion is in the low-spin t_{2g}^4 state with $S = 1$ and $L_z = 1$, and those occupied states are separated from other unoccupied Fe 3d states by electronic Coulomb correlations, which essentially determine the insulating behavior of FeS₂ monolayer, see Fig. 4(a). The negative charge-transfer character and strong Fe 3d-S 3p hybridization, both associated with the unusually high Fe⁴⁺ valence state, give rise to

broad bands which eventually reduce the above gap drastically to a minor semiconducting gap as seen in Figs. 4(b) and 4(c).

Indeed, the energy splitting between the L_{z+} and L_{z-} orbitals arises from the SOC effect. In addition to this, electron correlation plays a significant role in determining the energy splitting between the occupied and unoccupied Fe 3d states, as shown in Fig. 4(a). In this work, we stabilize the spin-orbital ground state and several metastable states using LSDA+SOC+ U calculations, where the ‘large’ energy splitting between the occupied and unoccupied Fe 3d states are always present due to the Hubbard U . In order to determine the spin-orbital excitation energy of the Fe 3d states, e.g., the L_{z+}/L_{z-} orbital splitting by SOC, we cannot use the DOS results but instead use the computed total energy differences as shown in Fig. 3(d). Our results show that the SOC L_{z+}/L_{z-} splitting is 61 meV, which just reflects the SOC strength ζ of the Fe 3d state. Actually, the ζ parameter of ionic Fe 3d state is known to be about 60-70 meV, and the present agreement reflects the good accuracy of our calculations.

After investigating all the spin-orbital states of the unusual high-valent and the LS Fe⁴⁺ ions, we find that the ground state is L_{z+} , see Fig. S5(a). It has the nominal large orbital moment of $1 \mu_B$ which is parallel to the total spin moment of $2 \mu_B$, and has a small insulating gap of 40 meV as shown in Fig. 4(c), which is in agreement with the observed small gap insulating behavior of FeS₂ monolayer [21]. Note that this small gap band structure (Fig. 4(c)) is also well reproduced by a hybrid functional calculation which yields a very similar band structure, as seen in Fig. S6 of SM [29]. Moreover, the L_{z+} ground state has a huge SIA energy of 25 meV/Fe and strongly favors the perpendicular magnetization. Therefore, FeS₂ monolayer could be an emerging 2D Ising magnet.

C. FM Couplings and High T_C

We now study the magnetic properties of FeS₂ monolayer. Besides the above calculated FM state, we also calculate three different AF states depicted in Fig. S7 of SM [29]. All the calculations are based on the LS L_{z+} spin-orbital ground state. The results show that the FM solution is the ground state and the three exchange parameters $J_1 = 5.81$ meV, $J_2 = 2.01$ meV, and $J_3 = 1.05$ meV are all FM, see section IV in SM for more details [29]. For 2D FM semiconductors and insulators, normally a superexchange plays a dominant role in establishing the magnetic couplings, and the hybridization between the magnetic transition-metal ions and the ligand ions has a strong impact on the strength of the superexchange couplings. The largest $J_1 = 5.81$ meV can be qualitatively explained by the charge-transfer type superexchange, and the large distance J_3 of 1.05 meV is still sizeable due to the strong Fe 3d-S 3p hybridization and the tiny band gap (in this unusually high valent system)

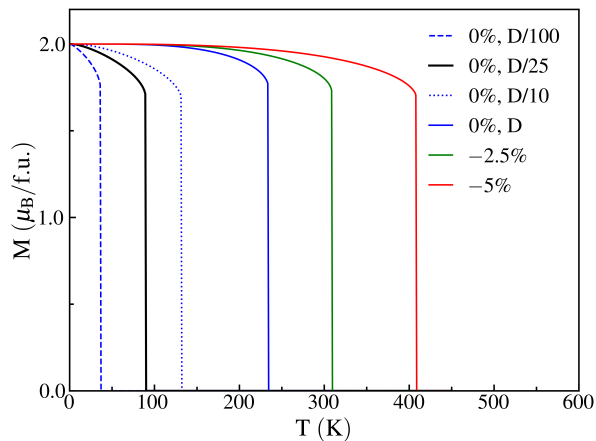


FIG. 5. The magnetization M as a function of temperature calculated by RSWT. Here the SIA parameter is $D=25$ meV. T_C is determined by $M = 0$.

both of which facilitate the long-range FM coupling. As FeS₂ monolayer is a tiny-gap charge-transfer semiconductor, the virtual excitations from S $3p$ to Fe $3d$ associated with the superexchange are energetically cheap. Moreover, the strong Fe $3d$ -S $3p$ hybridizations yield large hopping parameters. Then the two major superexchange channels, counting the large $pd\sigma$ and medium $pd\pi$ hybridizations, contribute to the FM J_1 coupling, for more details see Section V in SM [29].

Using the three FM exchange parameters and the huge SIA parameter $D = 25$ meV, here we perform RSWT calculations (see Section VI in SM [29]) and find that FeS₂ monolayer has a pretty high $T_C = 261$ K as seen in Fig. 5. In the RSWT calculations, the T_C is sensitive to the SIA energy, and T_C would drop a lot when the SIA parameter is reduced from the present huge value of 25 meV down to the more common few meV or tenths of meV: e.g., T_C is reduced to 132 K for SIA=2.5 meV, and down to 37 K for SIA=0.25 meV (see Fig. 5). These results show that the present huge SIA indeed contributes a lot to stabilize the pretty high $T_C = 261$ K. Note that when using the three FM parameters ($J_1 = 4.73$ meV, $J_2 = 1.33$ meV, and $J_3 = 1.27$ meV, see Table S7 in SM) and the unchanged $D = 25$ meV both obtained by LSDA+SOC+ U with $U = 6$ eV, the T_C is somewhat reduced to 234 K. When $U = 4$ eV is assumed, the small gap is closed, and the FM metallic solution gives a stronger itinerant FM behavior and higher $T_C > 261$ K (compared with $U = 5$ eV). Therefore, for the very reasonable $U = 5$ eV (or somewhat larger U) to open the experimental small gap of FeS₂ monolayer, the T_C is 261 K (or somewhat lower but it is still a pretty high T_C).

As the SIA arises from the LS L_{z+} ground state which benefits from the half-filled lower e_g^π doublet than the a_{1g} singlet in the global trigonal crystal field, one would expect that a biaxial compressive strain would force the FeS₆ octahedra to elongate along the global z -axis, i.e., along the local cubic [111] direction, and then enlarge

the crystal-field splitting between the lower e_g^π doublet and the higher a_{1g} singlet. As a result, the LS L_{z+} ground state, out of the lower e_g^π doublet, becomes even more stable, and the in-plane FM exchange could become stronger due to the shortened bond lengths. Upon the biaxial compressive strain, the energy separation between the L_{z+} ground state and the higher a_{1g} singlet is indeed increased as expected (see Fig. S9 in SM [29]), but under the tensile strain, the energy separation is reduced and even changes its sign when the tensile strain is larger than 2.5%. Moreover, under the compressive strain, the FM ground state gets more stable than other AF states, indicating a stronger FM exchange, see Section VII in SM for more details [29]. Then, using the enhanced FM exchanges and the huge SIA under the compressive strain, our RSWT calculations show that the T_C is increased from 261 K for the pristine FeS₂ monolayer to 310 K for the -2.5% strain, and to 409 K for the -5.0% strain, see Fig. 5. We also carry out MC simulations and find the T_C is comparable to the RSWT prediction. The corresponding T_C values are 220 K, 275 K, and 350 K according to our MC simulations, see Section VIII in SM [29]. Both sets of results arrive at the same conclusion that the pristine FeS₂ monolayer would have a pretty high T_C which is even above room temperature under a few percent compressive strain. Therefore, the emerging FeS₂ monolayer would be an appealing high- T_C 2D Ising ferromagnet.

D. Sulfur Vacancy

Now we comment on why the recent experimental T_C is only about 15 K [21]. It may well be due to the S vacancies. Such ligand vacancies are quite common in the high valent materials [26, 42, 43] and the 2D materials [44–47]. We have now performed DFT calculations using a 3×3 supercell with a single sulfur vacancy in our simulations (with the vacancy ratio of 1/18), see Fig. S12(a) in Section IX of SM [29]. The supercell structure is relaxed using LSDA, and we compare the total energies calculated by LSDA+SOC+ U for the spin orientation either out-of-plane or in-plane, and find that the magnetic anisotropy energy (MAE) still favors the easy out-of-plane but drops drastically down to only 1.02 meV/Fe on average. This drastic reduction of MAE is mainly due to a lifting of the orbital degeneracy by the lattice distortion associated with the sulfur vacancy, and the further crystal field splitting largely suppresses the orbital moment and the MAE. Note that the sulfur vacancy acts like an electron donor, and the minor gap in the otherwise vacancy free prototype material closes now, see Fig. S12(b) in SM. Moreover, owing to the sulfur vacancy and the lattice distortion, there exist many inequivalent Fe sites in the supercell, and there are even much more different magnetic exchange parameters. Here, we just make a crude estimate because of this complexity. For example, for the Fe site farthest away from the S vacancy, our LSDA+SOC+ U calculations give the averaged first-nearest neighboring

exchange parameter of 6.00 meV. This small increase of the FM coupling strength, compared with the above homogeneous $J_1 = 5.81$ meV, may well be due to the enhanced itineracy associated with the electron donation of the sulfur vacancy. However, for the Fe site closest to the S vacancy, our LSDA+SOC+ U calculations give the averaged first-nearest neighboring exchange parameter to be -5.70 meV, which even turns into an AF type due to the S vacancy. Therefore, the averaged exchange (most likely FM) among the many different magnetic channels in the supercell with the sulfur vacancy can be expected to be not stronger than those homogeneous ones in the ideal lattice. Taking the above J_1 , J_2 , and J_3 as the upper limit, solely the drastic decrease of the MAE already significantly reduces the T_C down to 90 K (see the solid black curve in Fig. 5). Such T_C would be further reduced (and approach the experimental 15 K) when the averagely decreasing FM exchange (and even AF type for some exchange channels) is used. Therefore, to achieve the ideal high T_C in FeS₂ monolayer, the S vacancy issue should be avoided during the sample preparation/growth, e.g., using the high pressure [48], post-growth treatment [49] and sulfur-rich growth [50].

IV. Summary

In summary, we propose FeS₂ monolayer to be an appealing 2D high- T_C Ising FM magnet, using density functional calculations, crystal field level analyses and spin-orbital-state diagrams, RSWT and MC simulations. Our results reveal that the unusual high valent Fe⁴⁺ is in the LS L_{z+} spin-orbital ground state, resulting in a large orbital moment of about $1 \mu_B$ and huge MA of 25 meV/Fe. The negative charge transfer character associated with the Fe high valence, strong Fe $3d$ -S $3p$ hybridization, wide bands but a small band gap all help to establish a strong FM superexchange. As the compressive strains can further stabilize the L_{z+} ground state and enhance the FM couplings, our RSWT simulations show that the T_C of FeS₂ monolayer is increased from 261 K for a bare monolayer up to 310~409 K under $-2.5\sim-5\%$ strains. This work highlights the exploration of the spin-orbital degrees of freedom to produce the strong Ising magnetism and FM coupling. This approach may pave the way for discovering more 2D high- T_C FM materials suitable for spintronic applications.

Acknowledgements

This work was supported by National Natural Science Foundation of China (Grants No. 12104307, No. 12174062, and No.12241402). K. Yang and Y. Ma contributed equally to this work.

-
- [1] B. Huang, G. Clark, E. Navarro-Moratalla, D. R. Klein, R. Cheng, K. L. Seyler, D. Zhong, E. Schmidgall, M. A. McGuire, D. H. Cobden, W. Yao, D. Xiao, P. Jarillo-Herrero, and X. Xu, Layer-dependent ferromagnetism in a van der Waals crystal down to the monolayer limit, *Nature* **546**, 270 (2017).
- [2] C. Gong, L. Li, Z. Li, H. Ji, A. Stern, Y. Xia, T. Cao, W. Bao, C. Wang, Y. Wang, Z. Q. Qiu, R. J. Cava, S. G. Louie, J. Xia, and X. Zhang, Discovery of intrinsic ferromagnetism in two-dimensional van der Waals crystals, *Nature* **546**, 265 (2017).
- [3] T. Li, S. Jiang, N. Sivadas, Z. Wang, Y. Xu, D. Weber, J. E. Goldberger, K. Watanabe, T. Taniguchi, C. J. Fennie, K. F. Mak, and J. Shen, Pressure-controlled interlayer magnetism in atomically thin CrI₃, *Nat. Mater.* **18**, 1303 (2019).
- [4] T. Song, Z. Fei, M. Yankowitz, Z. Lin, Q. Jiang, K. Hwangbo, Q. Zhang, B. Sun, T. Taniguchi, K. Watanabe, M. A. McGuire, D. Graf, T. Cao, J.-H. Chu, D. H. Cobden, C. R. Dean, D. Xiao, and X. Xu, Switching 2D magnetic states via pressure tuning of layer stacking, *Nat. Mater.* **18**, 1298 (2019).
- [5] J. Li, X. Yang, Y. Liu, B. Huang, R. Wu, Z. Zhang, B. Zhao, H. Ma, W. Dang, Z. Wei, K. Wang, Z. Lin, X. Yan, M. Sun, B. Li, X. Pan, J. Luo, G. Zhang, Y. Liu, Y. Huang, X. Duan, and X. Duan, General synthesis of two-dimensional van der Waals heterostructure arrays, *Nature* **579**, 368 (2020).
- [6] K. S. Burch, D. Mandrus, and J.-G. Park, Magnetism in two-dimensional van der Waals materials, *Nature* **563**, 47 (2018).
- [7] T. Song, X. Cai, M. W.-Y. Tu, X. Zhang, B. Huang, N. P. Wilson, K. L. Seyler, L. Zhu, T. Taniguchi, K. Watanabe, M. A. McGuire, D. H. Cobden, D. Xiao, W. Yao, and X. Xu, Giant tunneling magnetoresistance in spin-filter van der Waals heterostructures, *Science* **360**, 1214 (2018).
- [8] N. D. Mermin and H. Wagner, Absence of ferromagnetism or antiferromagnetism in one- or two-dimensional isotropic heisenberg models, *Phys. Rev. Lett.* **17**, 1133 (1966).
- [9] J. L. Lado and J. Fernández-Rossier, On the origin of magnetic anisotropy in two dimensional CrI₃, *2D Mater.* **4**, 035002 (2017).
- [10] C. Xu, J. Feng, H. Xiang, and L. Bellaiche, Interplay between Kitaev interaction and single ion anisotropy in ferromagnetic CrI₃ and CrGeTe₃ monolayers, *npj Comput. Mater.* **4**, 57 (2018).
- [11] D.-H. Kim, K. Kim, K.-T. Ko, J. Seo, J. S. Kim, T.-H. Jang, Y. Kim, J.-Y. Kim, S.-W. Cheong, and J.-H. Park, Giant magnetic anisotropy induced by ligand LS coupling in layered Cr compounds, *Phys. Rev. Lett.* **122**, 207201 (2019).

- (2019).
- [12] K. Yang, F. Fan, H. Wang, D. Khomskii, and H. Wu, VI_3 : A two-dimensional Ising ferromagnet, *Phys. Rev. B* **101**, 100402(R) (2020).
 - [13] Z. Lin, B. Huang, K. Hwangbo, Q. Jiang, Q. Zhang, Z. Liu, Z. Fei, H. Lv, A. Millis, M. McGuire, D. Xiao, J.-H. Chu, and X. Xu, Magnetism and its structural coupling effects in 2D Ising ferromagnetic insulator VI_3 , *Nano Lett.* **21**, 9180 (2021).
 - [14] Y. Hao, Y. Gu, Y. Gu, E. Feng, H. Cao, S. Chi, H. Wu, and J. Zhao, Magnetic order and its interplay with structure phase transition in van der Waals ferromagnet VI_3 , *Chin. Phys. Lett.* **38**, 096101 (2021).
 - [15] A. De Vita, T. T. P. Nguyen, R. Sant, G. M. Pierantozzi, D. Amoroso, C. Bigi, V. Polewczyk, G. Vinai, L. T. Nguyen, T. Kong, J. Fujii, I. Vobornik, N. B. Brookes, G. Rossi, R. J. Cava, F. Mazzola, K. Yamauchi, S. Picozzi, and G. Panaccione, Influence of orbital character on the ground state electronic properties in the van der Waals transition metal iodides VI_3 and CrI_3 , *Nano Lett.* **22**, 7034 (2022).
 - [16] K. Yang, G. Wang, L. Liu, D. Lu, and H. Wu, Triaxial magnetic anisotropy in the two-dimensional ferromagnetic semiconductor CrSBr , *Phys. Rev. B* **104**, 144416 (2021).
 - [17] D. Lu, L. Liu, Y. Ma, K. Yang, and H. Wu, A unique electronic state in a ferromagnetic semiconductor FeCl_2 monolayer, *J. Mater. Chem. C* **10**, 8009 (2022).
 - [18] C. Huang, J. Feng, F. Wu, D. Ahmed, B. Huang, H. Xiang, K. Deng, and E. Kan, Toward intrinsic room-temperature ferromagnetism in two-dimensional semiconductors, *J. Am. Chem. Soc.* **140**, 11519 (2018).
 - [19] F. Xue, Y. Hou, Z. Wang, and R. Wu, Two-dimensional ferromagnetic van der Waals CrCl_3 monolayer with enhanced anisotropy and Curie temperature, *Phys. Rev. B* **100**, 224429 (2019).
 - [20] L. Liu, K. Yang, G. Wang, and H. Wu, Two-dimensional ferromagnetic semiconductor VBr_3 with tunable anisotropy, *J. Mater. Chem. C* **8**, 14782 (2020).
 - [21] J. Zhou, C. Zhu, Y. Zhou, J. Dong, P. Li, Z. Zhang, Z. Wang, Y.-C. Lin, J. Shi, R. Zhang, Y. Zheng, H. Yu, B. Tang, F. Liu, L. Wang, L. Liu, G.-B. Liu, W. Hu, Y. Gao, H. Yang, W. Gao, L. Lu, Y. Wang, K. Suenaga, G. Liu, F. Ding, Y. Yao, and Z. Liu, Composition and phase engineering of metal chalcogenides and phosphorous chalcogenides, *Nat. Mater.* **22**, 450 (2023).
 - [22] M. M. Otrokov, I. I. Klimovskikh, H. Bentmann, D. Estyunin, A. Zeugner, Z. S. Aliev, S. Gass, A. U. B. Wolter, A. V. Koroleva, A. M. Shikin, M. Blanco-Rey, M. Hoffmann, I. P. Rusinov, A. Y. Vyazovskaya, S. V. Eremin, Y. M. Koroteev, V. M. Kuznetsov, F. Freyse, J. Sanchez-Barriga, I. R. Amiraslanov, M. B. Babanly, N. T. Mamedov, N. A. Abdullayev, V. N. Zverev, A. Alfonsov, V. Kataev, B. Buechner, E. F. Schwier, S. Kumar, A. Kimura, L. Petaccia, G. Di Santo, R. C. Vidal, S. Schatz, K. Kissner, M. Uenzelmann, C. H. Min, S. Moser, T. R. F. Peixoto, F. Reinert, A. Ernst, P. M. Echenique, A. Isaeva, and E. V. Chulkov, Prediction and observation of an antiferromagnetic topological insulator, *Nature* **576**, 416 (2019).
 - [23] Y. Deng, Y. Yu, M. Z. Shi, Z. Guo, Z. Xu, J. Wang, X. H. Chen, and Y. Zhang, Quantum anomalous Hall effect in intrinsic magnetic topological insulator MnBi_2Te_4 , *Science* **367**, 895 (2020).
 - [24] H. Seki, Y. Hosaka, T. Saito, M. Mizumaki, and Y. Shimakawa, Ferromagnetism induced by substitution of the iron(IV) ion by an unusual high-valence nickel(IV) ion in antiferromagnetic SrFeO_3 , *Angew. Chem., Int. Ed.* **55**, 1360 (2016).
 - [25] Y. Hosaka, N. Ichikawa, T. Saito, P. Manuel, D. Khalyavin, J. P. Attfield, and Y. Shimakawa, Two-dimensional charge disproportionation of the unusual high valence state Fe^{4+} in a layered double perovskite, *J. Am. Chem. Soc.* **137**, 7468 (2015).
 - [26] M. Goto, T. Oguchi, and Y. Shimakawa, Geometrical spin frustration and monoclinic-distortion-induced spin canting in the double perovskites $\text{Ln}_2\text{LiFeO}_6$ ($\text{Ln} = \text{La}, \text{Nd}, \text{Sm}, \text{and Eu}$) with unusually high valence Fe^{5+} , *J. Am. Chem. Soc.* **143**, 19207 (2021).
 - [27] G. Kresse and J. Hafner, Ab initio molecular dynamics for liquid metals, *Phys. Rev. B* **47**, 558(R) (1993).
 - [28] J. P. Allen and G. W. Watson, Occupation matrix control of d- and f-electron localisations using DFT + U, *Phys. Chem. Chem. Phys.* **16**, 21016 (2014).
 - [29] See Supplemental Material at <http://link.aps.org/supplemental/> for more details on (I) the trigonal crystal field and orbital state, (II) the LSDA+SOC+U results, (III) hybrid functional results, (IV) the exchange parameters, (V) two major superexchange channels, (VI) the renormalized spin-wave theory (RSWT), (VII) strain results, (VIII) the Monte Carlo (MC) simulations, and (IX) the sulfur vacancy calculations. The Supplemental Material also contains Refs. [21, 30-37].
 - [30] P. Blaha, K. Schwarz, F. Tran, R. Laskowski, G. K. H. Madsen, and L. D. Marks, Wien2k: An APW+lo program for calculating the properties of solids, *J. Chem. Phys.* **152**, 074101 (2020).
 - [31] A. D. Becke, A new mixing of Hartree-Fock and local density-functional theories, *J. Chem. Phys.* **98**, 1372 (1993).
 - [32] A. D. Becke, Density-functional thermochemistry. IV. a new dynamical correlation functional and implications for exact-exchange mixing, *J. Chem. Phys.* **104**, 1040 (1996).
 - [33] J. P. Perdew, M. Ernzerhof, and K. Burke, Rationale for mixing exact exchange with density functional approximations, *J. Chem. Phys.* **105**, 9982 (1996).
 - [34] F. Tran, P. Blaha, K. Schwarz, and P. Novák, Hybrid exchange-correlation energy functionals for strongly correlated electrons: Applications to transition-metal monoxides, *Phys. Rev. B* **74**, 155108 (2006).
 - [35] P. Novák, J. Kuneš, L. Chaput, and W. E. Pickett, Exact exchange for correlated electrons, *Phys. Status Solidi B* **243**, 563 (2006).
 - [36] Z. Li, T. Cao, and S. G. Louie, Two-dimensional ferromagnetism in few-layer van der Waals crystals: Renormalized spin-wave theory and calculations, *Journal of Magnetism and Magnetic Materials* **463**, 28 (2018).
 - [37] N. Metropolis and S. Ulam, The Monte Carlo method, *J. Am. Stat. Assoc.* **44**, 335 (1949).
 - [38] Q. Yao, J. Li, and Q. Liu, Fragile symmetry-protected half metallicity in two-dimensional van der Waals magnets: A case study of monolayer FeCl_2 , *Phys. Rev. B* **104**, 035108 (2021).
 - [39] X. Ou, H. Wang, F. Fan, Z. Li, and H. Wu, Giant magnetic anisotropy of Co, Ru, and Os adatoms on MgO (001) surface, *Phys. Rev. Lett.* **115**, 257201 (2015).

- [40] T. Mizokawa, H. Namatame, A. Fujimori, K. Akeyama, H. Kondoh, H. Kuroda, and N. Kosugi, Origin of the band gap in the negative charge-transfer-energy compound NaCuO_2 , *Phys. Rev. Lett.* **67**, 1638 (1991).
- [41] V. Bisogni, S. Catalano, R. J. Green, M. Gibert, R. Scherwitzl, Y. Huang, V. N. Strocov, P. Zubko, S. Balandeh, J.-M. Triscone, G. Sawatzky, and T. Schmitt, Ground-state oxygen holes and the metal-insulator transition in the negative charge-transfer rare-earth nickelates, *Nat. Commun.* **7**, 13017 (2016).
- [42] R. B. Wexler, G. S. Gautam, E. B. Stechel, and E. A. Carter, Factors governing oxygen vacancy formation in oxide perovskites, *J. Am. Chem. Soc.* **143**, 13212 (2021).
- [43] C. Lu and J.-M. Liu, The $\text{jeff} = 1/2$ antiferromagnet Sr_2IrO_4 : a golden avenue toward new physics and functions, *Adv. Mater.* **32**, 1904508 (2020).
- [44] L. Wang, X. Zhang, H. L. Chan, F. Yan, and F. Ding, Formation and healing of vacancies in graphene chemical vapor deposition (CVD) growth, *J. Am. Chem. Soc.* **135**, 4476 (2013).
- [45] H. Wang, D. Yong, S. Chen, S. Jiang, X. Zhang, W. Shao, Q. Zhang, W. Yan, B. Pan, and Y. Xie, Oxygen-vacancy-mediated exciton dissociation in BiOBr for boosting charge-carrier-involved molecular oxygen activation, *J. Am. Chem. Soc.* **140**, 1760 (2018).
- [46] T. Kong, K. Stolze, E. I. Timmons, J. Tao, D. Ni, S. Guo, Z. Yang, R. Prozorov, and R. J. Cava, VI_3 —a new layered ferromagnetic semiconductor, *Adv. Mater.* **31**, 1808074 (2019).
- [47] D. Ni, X. Gui, K. M. Powderly, and R. J. Cava, Honeycomb-structure RuI_3 , a new quantum material related to $\alpha\text{-RuCl}_3$, *Adv. Mater.* **34**, 2106831 (2022).
- [48] L. Yan, J. Qin, B. Liang, S. Gao, B. Wang, J. Cui, A. Bolag, and Y. Yang, High pressure rapid synthesis of LiCrTiO_4 with oxygen vacancy for high rate lithium-ion battery anodes, *Small* **18**, 2202901 (2022).
- [49] X. Zhao, P. Song, C. Wang, A. C. Riis-Jensen, W. Fu, Y. Deng, D. Wan, L. Kang, S. Ning, J. Dan, T. Venkatesan, Z. Liu, W. Zhou, K. S. Thygesen, X. Luo, S. J. Pennycook, and K. P. Loh, Engineering covalently bonded 2D layered materials by self-intercalation, *Nature* **581**, 171 (2020).
- [50] X. Zheng, A. Calò, T. Cao, X. Liu, Z. Huang, P. M. Das, M. Drndic, E. Albisetti, F. Lavini, T.-D. Li, V. Narang, W. P. King, J. W. Harrold, M. Vittadello, C. Aruta, D. Shahrjerdi, and E. Riedo, Spatial defects nanoengineering for bipolar conductivity in MoS_2 , *Nat. Commun.* **11**, 3463 (2020).

Supplemental Material for "FeS₂ monolayer: a high valence and high- T_C Ising ferromagnet"

I. The trigonal crystal field and orbital state in FeS₂ monolayer

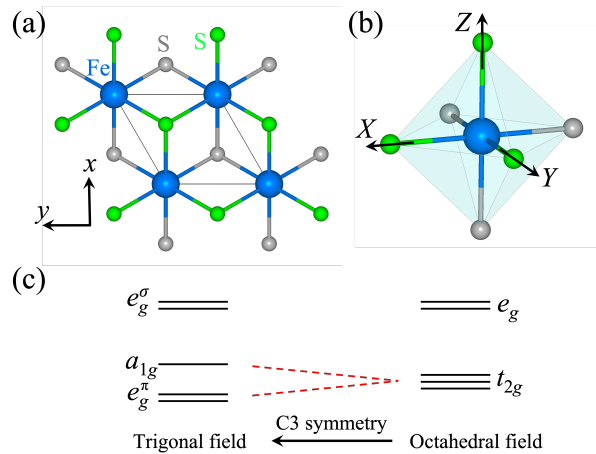


Fig. S1. (a) The crystal structure of the newly synthesized monolayer phase FeS₂ in the global xyz coordinate system. (b) The local FeS₆ octahedron in its local XYZ coordination system. (c) The Fe 3d orbital states in the local octahedral but global trigonal crystal field.

The crystal structure of the newly synthesized FeS₂ monolayer in the $P\bar{3}m1$ space group [21] features local octahedral coordination of Fe ions and a trigonal crystal field in the global coordinate system. This crystal field splits the degenerate t_{2g} triplet into the a_{1g} singlet and e_g^π doublet. In the following calculations, we use the global coordinate system with the z axis along the $[111]$ direction of the local FeS₆ octahedra and the y axis along the $[1\bar{1}0]$ direction (the x -axis is uniquely defined and the xy plane is in the hexagonal ab plane). Then the Fe 3d wave functions under the global xyz coordinate system in trigonal crystal field can be written as

$$\begin{aligned}
 |a_{1g}\rangle &= |3z^2 - r^2\rangle \\
 |e_{g1}^\pi\rangle &= \sqrt{\frac{2}{3}}|x^2 - y^2\rangle - \sqrt{\frac{1}{3}}|xz\rangle \\
 |e_{g2}^\pi\rangle &= \sqrt{\frac{1}{3}}|yz\rangle + \sqrt{\frac{2}{3}}|xy\rangle \\
 |e_{g1}^\sigma\rangle &= \sqrt{\frac{1}{3}}|x^2 - y^2\rangle + \sqrt{\frac{2}{3}}|xz\rangle \\
 |e_{g2}^\sigma\rangle &= \sqrt{\frac{2}{3}}|yz\rangle - \sqrt{\frac{1}{3}}|xy\rangle
 \end{aligned} \tag{S1}$$

When the SOC is considered, different linear combinations of the a_{1g} singlet and e_g^π doublet yield the $L = 1$

orbital moment:

$$\begin{aligned}
|L_{z\pm}\rangle &= \frac{1}{\sqrt{2}} (|e_{g1}^\pi\rangle \pm i |e_{g2}^\pi\rangle) \\
|L_{x\pm}\rangle &= \frac{1}{\sqrt{2}} (|e_{g2}^\pi\rangle \pm i |a_{1g}\rangle) \\
|L_{y\pm}\rangle &= \frac{1}{\sqrt{2}} (|e_{g1}^\pi\rangle \pm i |a_{1g}\rangle)
\end{aligned} \tag{S2}$$

where $L_{x,y,z}$ represents the orientation of the orbital moment along the x , y , and z axes, and \pm stands for the $L_i = \pm 1$. Owing to the degeneracy of the e_g^π doublet in the trigonal crystal field, the L_x and L_y states are still degenerate.

II. The LSDA+SOC+ U DOS results for the different spin-orbital states

Table S1. Relative total energies ΔE (meV/fu), local spin and orbital moments (μ_B) in different spin-orbital states calculated by LSDA+SOC+ U with $U = 5$ eV. The symbols \perp (\parallel) stand for the out-of-plane (in-plane) magnetization.

States	ΔE	Fe _{spin}	Fe _{orb}
$L_{z+} \perp$	0	1.98	0.94
$L_{z+} \parallel$	25	1.98	0.27
$L_{x+} \parallel$	42	2.00	1.00
$a_{1g} \parallel$	44	1.88	0.28
$L_{z-} \perp$	61	1.99	-0.84

Table S2. Relative total energies ΔE (meV/fu), local spin and orbital moments (μ_B) in different spin-orbital states calculated by LSDA+SOC+ U with $U = 6$ eV. The symbols \perp (\parallel) stand for the out-of-plane (in-plane) magnetization.

States	ΔE	Fe _{spin}	Fe _{orb}
$L_{z+} \perp$	0	2.10	1.03
$L_{z+} \parallel$	25	2.12	0.38

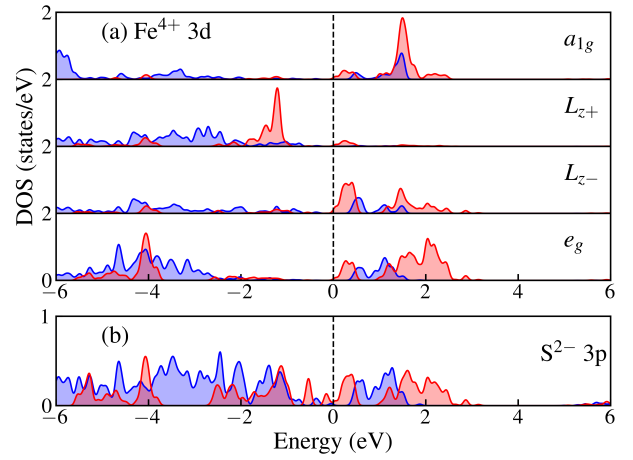


Fig. S2. (a) Fe 3d and (b) S 3p DOS for $L_{z+} \parallel$ state. The blue (red) curves stand for the up (down) spin channel.

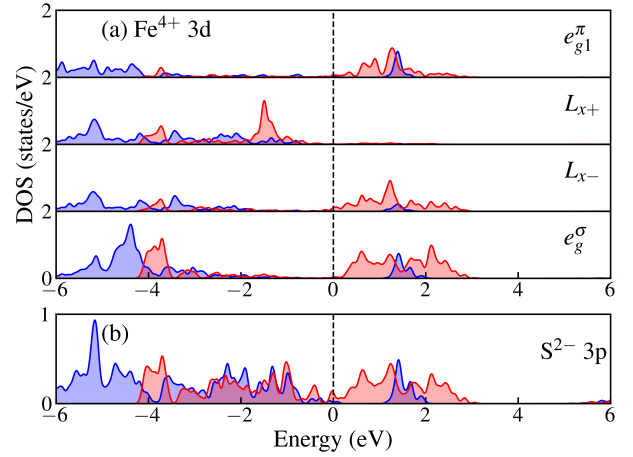


Fig. S3. (a) Fe 3d and (b) S 3p DOS for $L_{x+} \parallel$ state.

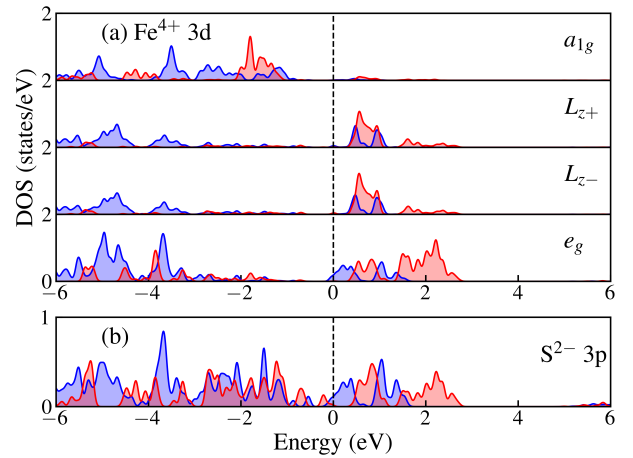


Fig. S4. (a) Fe 3d and (b) S 3p DOS for $a_{1g} \parallel$ state.

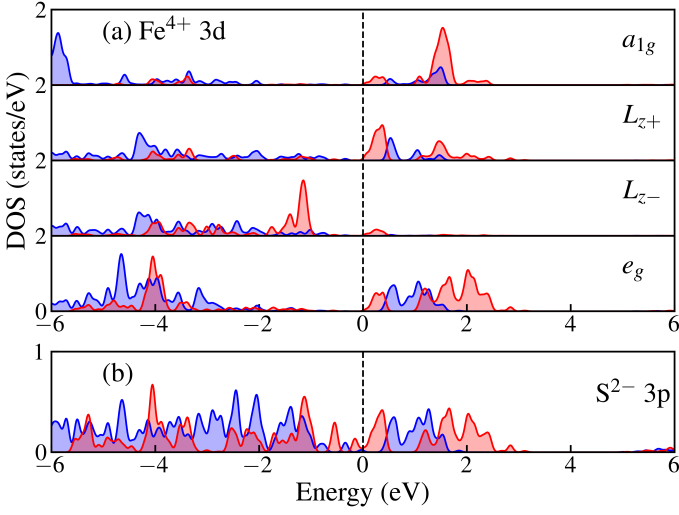


Fig. S5. (a) Fe 3d and (b) S 3p DOS for L_{z-} state.

III. The hybrid functional band calculations

The hybrid functional band structure for the FeS_2 monolayer is calculated using the full-potential augmented plane wave plus local orbital code (WIEN2K)[30]. The muffin-tin sphere radii are chosen to be 2.2 and 2.0 bohrs for Fe, and S atoms, respectively. The cutoff energy of 12 Ry is used for plane wave expansion. To account for the electron correlation effect of Fe 3d electrons, we employ a hybrid functional with a quarter Hartree-Fock exchange mixed into LSDA[31–35]. SOC is included by the second variational method with scalar relativistic wave functions, and the magnetization direction is set along the c -axis.

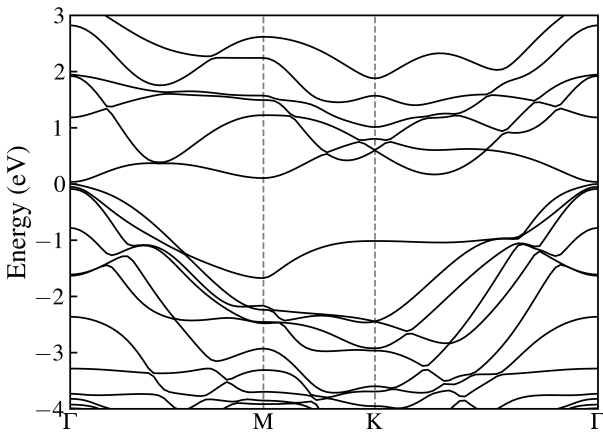


Fig. S6. The calculated band structure with a tiny band gap of 36 meV by hybrid functional calculation.

IV. The exchange parameters

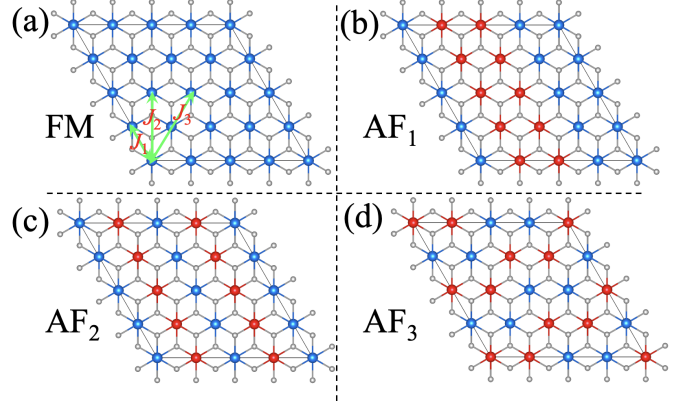


Fig. S7. The four common commensurate magnetic structures of FeS_2 monolayer. The blue (red) balls stand for the up (down) spin Fe ions.

In order to study the magnetic properties of the FeS_2 monolayer, a 4×4 supercell is selected within the LSDA+SOC+ U framework. The four common magnetic structures are used to estimate the three exchange parameters: J_1 , J_2 , and J_3 , see Fig S7(a). The results show that the FM solution is the most stable and has a lower total energy than the three antiferromagnetic (AF) states by 24~32 meV/f.u., see Table S4. Counting $-JS^2$ for each pair of LS Fe^{4+} $S = 1$ ions (positive J refers to FM exchange), the magnetic exchange energies of the FM state and the three AF states per formula unit are written as follows:

$$\begin{aligned}
 E_{\text{FM}} &= (-3J_1 - 3J_2 - 3J_3)S^2 \\
 E_{\text{AF}_1} &= (-J_1 + J_2 + J_3)S^2 \\
 E_{\text{AF}_2} &= (+J_1 + J_2 - 3J_3)S^2 \\
 E_{\text{AF}_3} &= (+J_1 - J_2 + J_3)S^2
 \end{aligned} \tag{S3}$$

Table S3. Relative total energies ΔE (meV/fu), local spin and orbital moments (μ_B) for the FeS_2 monolayer by LSDA+ U +SOC with $U = 5$ eV. The derived three exchange parameters $J_1 = 5.81$ meV, $J_2 = 2.01$ meV, and $J_3 = 1.05$ meV are all FM.

States	ΔE	Fe_{spin}	Fe_{orb}
FM	0	1.97	0.94
AF ₁	24.23	±1.95	±1.05
AF ₂	31.64	±1.91	±1.09
AF ₃	31.65	±1.95	±1.03

Table S4. Relative total energies ΔE (meV/fu), local spin and orbital moments (μ_B) for the FeS₂ monolayer by LSDA+ U +SOC with $U = 6$ eV. The derived three exchange parameters $J_1 = 4.73$ meV, $J_2 = 1.33$ meV, and $J_3 = 1.27$ meV are all FM.

States	ΔE	Fe _{spin}	Fe _{orb}
FM	0	2.06	1.03
AF ₁	19.91	±2.10	±1.12
AF ₂	24.30	±2.03	±1.11
AF ₃	26.71	±2.08	±1.15

V. Two major superexchange channels

The two major superexchange channels, counting the large $pd\sigma$ and medium $pd\pi$ hybridizations, contribute to the FM J_1 coupling. One arises from $pd\pi$ hybridization via the same p_Y orbital (but in an opposite spin orientation, figs. S8(a) and (c)), and the other involves the $pd\sigma$ hybridization via the orthogonal (p_X , p_Y) orbitals (Figs. S8(b) and (c)).

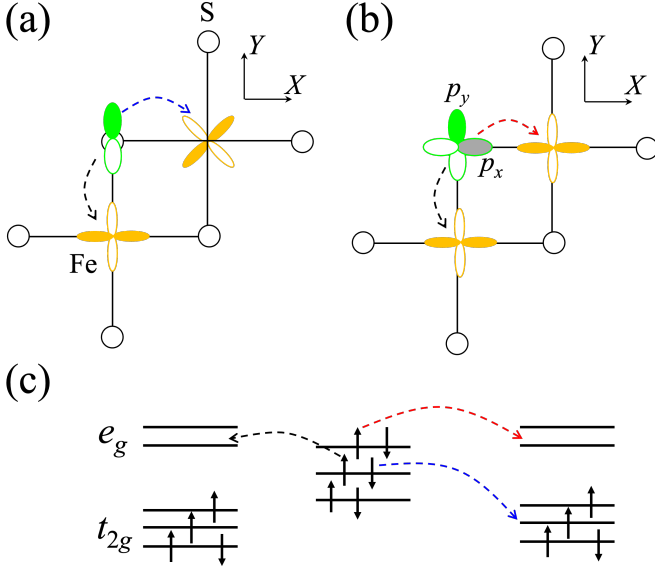


Fig. S8. Schematic plot of the (near-) 90° FM superexchange channels: (a) (XY) - p_Y - $(X^2 - Y^2)$, and (b) $(X^2 - Y^2)$ - (p_X, p_Y) - $(X^2 - Y^2)$.

VI. The renormalized spin-wave theory (RSWT) to simulate the T_C

We determine the T_C of FeS₂ monolayer with renormalized spin-wave theory[36]. One of the key advantages of using the renormalized spin-wave theory (RSWT) to simulate the critical temperature (T_C) of a magnetic material is its ability to take into account the effects of quan-

tum and thermal fluctuations on the spin waves. These effects are often neglected in the standard spin-wave theory, but they can have a significant impact on the behavior of magnetic materials at low temperatures. By accurately accounting for these effects, RSWT can provide more accurate predictions of T_C for a wide range of magnetic materials, including itinerant and localized systems, as well as materials with different types of spin interactions. This can be useful for understanding the magnetic properties of these materials and for designing new magnetic materials with desired properties. Additionally, RSWT is a relatively simple and computationally efficient approach, which makes it suitable for analyzing large systems and for performing parametric studies. This can be useful for exploring the effects of different factors on the critical temperature, such as the strength of the spin interactions or the presence of disorder in the material.

The spin operator \mathbf{S}_{lv} on site v of l th unit cell can be mapped into creation and annihilation operators of magnon by Holstein-Primakoff transformation. In the linear spin-wave theory(LSWT), which is the linear approximation of the Hamiltonian, the spin operators are mapped by linear term of Holstein-Primakoff transformation, i.e. $S_{lv}^+ \approx \sqrt{2S}a_{lv}$, $S_{lv}^- \approx \sqrt{2S}a_{lv}^\dagger$ and $S_{lv}^z = S - a_{lv}^\dagger a_{lv}$. Thus, the Hamiltonian, which only contains one-body operators, can be solved by Fourier transformation and matrix diagonalization. In the basis of LSWT, RSWT contains the second order approximation of Hamiltonian, where spin operators are mapped by second order approximated Holstein-Primakoff transformation

$$\begin{aligned}
 S_{lv}^+ &\approx \sqrt{2S} \left(a_{lv} - \frac{a_{lv}^\dagger a_{lv} a_{lv}}{4S} \right) \\
 S_{lv}^- &\approx \sqrt{2S} \left(a_{lv}^\dagger - \frac{a_{lv}^\dagger a_{lv}^\dagger a_{lv}}{4S} \right) \\
 S_{lv}^z &= S - a_{lv}^\dagger a_{lv}.
 \end{aligned} \tag{S4}$$

We define the number operator $\langle n_{kv} \rangle$, where k is wave vector in Fourier transformation, as our mean-field order parameter. Under Hartree-Fork approximation, we can diagonalize the Hamiltonian and obtain the self-consistent equation, which can be solved recursively. And following the Bose-Einstein statistics, the magnetization is expressed as

$$\frac{M}{M_0} = 1 - \frac{1}{nNS} \sum_k \langle n_k \rangle. \tag{S5}$$

VII. The strain results calculated by LSDA+SOC+U

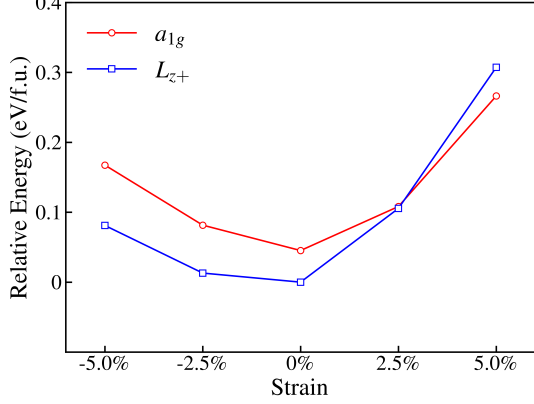


Fig. S9. The relative total energy (eV/f.u.) of the L_{z+} ground state against the a_{1g} state under different strains.

Table S5. Relative total energies ΔE (meV/fu), local spin and orbital moments (μ_B), and total spin moments (μ_B /fu) for different states of FeS₂ under different strain calculated by LSDA+SOC+U. The perpendicular magnetization is assumed in most cases, and the in-plane (\parallel) magnetization is also set for some cases.

Strain	States	ΔE	Fe _{spin}	Fe _{orb}	S _{spin}	Total _{spin}
-5%	L_{z+}	0	1.82	0.92	0.03	1.92
	$L_{z+} \parallel$	26	1.76	0.11 (x)	0.04	1.87
	a_{1g}	86	1.87	0.03	0.02	1.97
-2.5%	L_{z+}	0	1.84	0.95	0.02	1.91
	$L_{z+} \parallel$	27	1.85	0.23 (x)	0.02	1.91
	a_{1g}	69	1.76	-0.04	0.02	1.82
0%	L_{z+}	0	1.98	0.94	0.00	2.00
	$L_{z+} \parallel$	25	1.98	0.27 (x)	-0.01	1.99
	a_{1g}	45	1.84	0.05	-0.01	1.82
2.5%	L_{z+}	0	2.03	0.87	-0.02	1.99
	a_{1g}	3	1.84	-0.02	-0.02	1.82
5%	a_{1g}	0	1.84	0.01	-0.03	1.81
	L_{z+}	41	2.10	0.75	-0.05	1.98

Table S6. Relative total energies ΔE (meV/fu), local spin and orbital moments (μ_B) and total spin moments (μ_B /fu) for the FeS₂ monolayer under compressive strain by LSDA+U+SOC.

Strain	States	ΔE	Fe _{spin}	Fe _{orb}	S _{spin}	Total _{spin}
0%	FM	0	1.97	0.94	-0.001	1.98
	AF ₁	24.23	± 1.95	± 1.05	∓ 0.04	0.00
	AF ₂	31.64	± 1.91	± 1.09	∓ 0.01	0.00
	AF ₃	31.65	± 1.95	± 1.03	∓ 0.01	0.00
-2.5%	FM	0	1.83	0.96	-0.017	1.89
	AF ₁	31.91	± 1.86	± 1.09	∓ 0.013	0.00
	AF ₂	29.14	± 1.81	± 1.09	∓ 0.003	0.00
	AF ₃	41.81	± 1.83	± 1.10	∓ 0.011	0.00
-5%	FM	0	1.87	0.91	-0.030	1.97
	AF ₁	50.57	± 1.79	± 1.07	∓ 0.007	0.00
	AF ₂	48.89	± 1.76	± 1.11	∓ 0.001	0.00
	AF ₃	43.83	± 1.70	± 0.98	∓ 0.001	0.00

VIII. The Monte Carlo (MC) simulations

We perform a Monte Carlo (MC) simulation to simulate the thermal dynamic behavior and estimate the critical temperature. To choose a reasonable lattice size, three kinds of lattices are constructed in the simulations: $10 \times 10 \times 1$, $15 \times 15 \times 1$ and $20 \times 20 \times 1$. In each simulation, we use 8000 Monte Carlo steps to relax the system and then 15000 Monte Carlo steps to count magnetic moments. During the simulation step, each spin is rotated randomly in the three-dimensional space. The spin dynamical process is studied by the classical Metropolis methods [37]. And in each Monte Carlo step, more than 6000 spins are flipped. These simulations show that $15 \times 15 \times 1$ lattice is large enough for the simulation.

With the above study of the FM coupling and the giant perpendicular MA, we now assume the following spin Hamiltonian and carry out Monte Carlo simulations

$$H = - \sum_{k=1,2,3} \sum_{\langle ij \rangle} J_k \mathbf{S}_i \cdot \mathbf{S}_j - \sum_i D (S_i^z)^2 \quad (\text{S6})$$

where the first term describes the Heisenberg isotropic exchange (FM when $J > 0$), the second term is the SIA with the easy magnetization z axis (when $D \neq 0$), and $S_i = 1$ for the LS Fe⁴⁺ in the FeS₂ monolayer. Then, using the exchange parameters ($J_1 = 5.81$ meV, $J_2 = 2.01$ meV, and $J_3 = 1.05$ meV) and the MA energy ($D = 25$ meV), our Monte Carlo simulations show that T_C is 220 K for the FeS₂ monolayer, see Fig. S10.

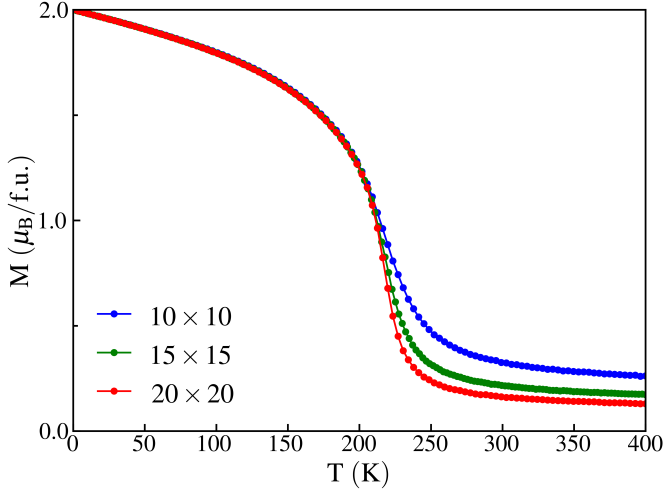


Fig. S10. Monte Carlo simulation of magnetization for FeS_2 monolayer in the $10 \times 10 \times 1$, $15 \times 15 \times 1$, and $20 \times 20 \times 1$ lattices.

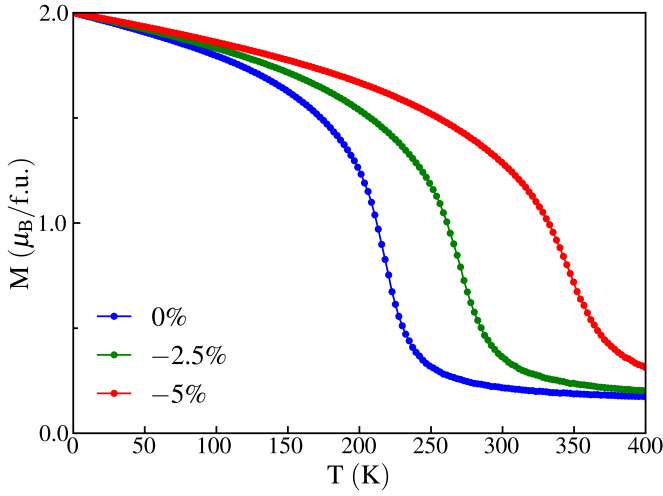


Fig. S11. Monte Carlo simulation of magnetization for FeS_2 monolayer in the $15 \times 15 \times 1$ lattice under different compressive strains. The T_C is increased from 220 K for a bare monolayer up to 275~350 K under -2.5~-5% strains.

IX. The sulfur vacancy calculations

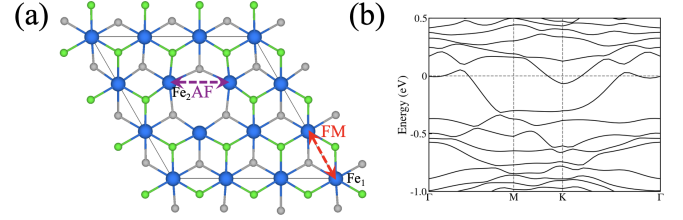


Fig. S12. (a) The 3×3 supercell of FeS_2 with a single sulfur vacancy (with the vacancy ratio of $1/18$). Our LSDA+SOC+ U calculations show: for the Fe_1 site farthest from the vacancy, the averaged exchange parameter is 6.00 meV for the first-nearest neighboring FM couplings; for the Fe_2 site nearest to the vacancy, the averaged exchange parameter is -5.70 meV for the first-nearest neighboring AF couplings. (b) The corresponding band structure for the FeS_2 with sulfur vacancy.